Received: 29 July 2022 | Revised: 27 September 2022 | Accepted: 2 October 2022

DOI: 10.1002/bte2.20220032

RESEARCH ARTICLE

BATTERY ENERGY Open Access WILEY

Rational design of PANI-modified three-dimensional dendritic hierarchical porous Cu–Sn nanocomposites as thick anodes with ultrahigh areal capacity and good cycling stability

Wenbo Liu[1] | **Hongmei Gou**[1] | **Xin Dong**[1] | **Shichao Zhang**[2] | **Sanqiang Shi**[3]

[1]School of Mechanical Engineering, Sichuan University, Chengdu, China

[2]School of Materials Science and Engineering, Beihang University, Beijing, China

[3]Department of Mechanical Engineering, The Hong Kong Polytechnic University, Hung Hom, Hong Kong, China

Correspondence
Wenbo Liu, School of Mechanical Engineering, Sichuan University, Chengdu 610065, China.
Email: liuwenbo_8338@163.com

Funding information

National Natural Science Foundation of China, Grant/Award Numbers: 52075351, 51604177; National Key Research and Development Program of China, Grant/Award Number: 2019YFA0705701; International S&T Innovation Cooperation Program of Sichuan Province, Grant/Award Number: 2020YFH0039; Chengdu International S&T Cooperation Funded Project, Grant/Award Number: 2022-GH02-00027-HZ: 2020-GH02-00006-HZ; "1000 Talents Plan" of Sichuan Province; Experimental Technology Project of Sichuan University, Grant/Award Number: SCU201078; Talent Introduction Program of Sichuan University, Grant/Award Number: YJ201410

Abstract

A simple and effective one-step strategy gives freestanding 3D dendritic hierarchical porous (DHP) Cu–Sn nanocomposites by chemically dealloying a designed $Cu_{35}Sn_{65}$ (at.%) alloy with dendritic segregation in a specific corrosive solution. A 3D DHP Cu–Sn modified by polyaniline (PANI) further makes the nanocomposites with improved conductivity and structural stability, which are typical of bimodal pore-size distribution comprising a dendritic micron-sized ligament-channel structure with interconnected nanoporous channel walls. The as-prepared 12 h dealloyed 3D DHP nanocomposites with ca. 200 μm in thickness can serve as binder-free thick anodes for lithium-ion batteries (LIBs) and exhibit enhanced Li storage performance with a ultrahigh first reversible capacity of 13.9 mAh cm^{-2} and an initial CE of 85.8%, good cycling stability with a capacity retention of 73.5% after 50 cycles, and superior rate capability with a reversible capacity of 11.95 mAh cm^{-2} after high-rate cycling. These Sn-based anodes can effectively alleviate the volume variation, enhance the loading of active materials, strengthen the stability of solid electrolyte interphase films, shorten the Li^+ migration distance, and improve the electron conductivity. Additionally, the Sn content and areal capacity of the 3D DHP electrode can be tuned by changing the dealloying time of the initial alloy for 3D tin-based thick anodes with adjustable capacities toward high-performance LIBs.

KEYWORDS

dendritic segregation, hierarchical porous structure, PANI-modified Cu–Sn nanocomposite, thick anode, tunable Sn content

1 | INTRODUCTION

With the rapid development of high-efficiency electrochemical energy-storage devices,[1–5] nowadays, lithium-ion batteries (LIBs) have been widely applied in various industrial and civil fields, such as mobile phones, laptops, electric vehicles, smart grids, and so on.[6–8] However, current anode and cathode materials hardly meet the expected demands of energy and power densities in future energy-storage systems due to extremely limited specific capacities.[9,10] Especially, it would be always unsatisfactory for an insertion-type commercial graphite anode to deliver the sluggish capacity of just less than 372 mAh g^{-1} and possess much low lithiation potential largely prone to dendritic precipitation of metal Li, which would easily bring about terrible electrochemical properties and poor safety.[11–13] As a result, seeking replaceable anode materials with higher specific capacity and more appropriate lithiation potential would be a primary challenge for next-generation LIBs, such as developed conversion-type and alloying-type anode materials in recent years.[14] Among them, metal tin has attracted extensive attention as a quite promising alloying-type anode candidate in advanced LIBs due to its high theoretical specific capacity (994 mAh g^{-1}, 2–3 times greater than commercial graphite), proper lithiation potential, abundant resources, environmentally friendly properties, and low cost.[15–19] Unfortunately, up to now, industrial development of tin-based anode materials still is impeded severely owing to its drastic volume and structure changes (200%–300%) during repetitive charge–discharge processes, which would give rise to quick cracking, serious mechanical separation, and perishing electrochemical performance.[20–25]

To overcome these problems, lots of productive strategies have been proposed and carried out successively in recent studies, such as reducing the feature size of active materials to the nanoscale, constructing active/inactive composite systems, and adopting 3D nanostructured substrates.[26–30] Typically, compared to traditional 2D planar counterparts, 3D nanostructured substrates with ample inner voids can effectively accommodate huge volume variation during repeated lithiation–delithiation processes, enhancing the structural stability and mechanical integrity of electrodes by changing the distribution of mechanical strain on electrode surfaces. Especially, 3D nanoporous metals (NPMs) with a quasiperiodic bicontinuous ligament-channel structure recently exhibit a great potential to act as both a current collector and substrate of anodes in LIBs, which can be prepared more easily by a dealloying technique than complex template-assisted methods previously.[19,31–33] For example, Zhang et al. reported a 3D Sn film-coated nanoporous copper (NPC) anode by dealloying and electroless deposition, which displays good Li storage properties with a first charge capacity of 1.68 mAh cm^{-2} and ca. 37% capacity retention after 50 cycles.[34] Liu et al. prepared a 3D-NPC-supported Sn NP anode with a first reversible capacity of 0.485 mAh cm^{-2} and a 52.4% capacity retention after 500 long cycles by dealloying and low-temperature deposition.[35] Note that Sn NPs can attain markedly better cycling stability than films due to more nanovoids around them to buffer volume change, whereas their areal specific capacity has to be killed largely in view of their extremely limited loadings. As a result, there seems to be an apparent conflict between areal capacity and cycling stability for Sn deposition on 3D porous skeletons. Until now, this still is a tough challenge to achieve their balance. On the other hand, constructing active/inactive composite NPs, such as Cu–Sn, Ni–Sn, and so on, is also an effective way to further improve the electrochemical performance of tin because the inactive component can serve as a cushion around tin to relieve its volume expansion and particle aggregation during cycling.[36–38] Thus, integrating 3D porous electrode structures and active/inactive composite NPs and building 3D porous electrodes composed of (rather than coated by) Cu–Sn alloy NPs might be a feasible route to achieve satisfactory electrochemical properties, in which the 3D porous framework with higher tin content would contribute to larger areal capacity, while small-sized Cu–Sn alloy NPs with abundant nanovoids and inactive components could bring about desirable cycling performance. Additionally, it has been known that conductive polymer coating considerably facilitates to stabilize solid electrolyte interphase (SEI) films and boosts structural stability, which can further improve coulombic efficiency (CE) and electron conductivity.[39–42]

In this report, a facile and effective one-step route has been developed to fabricate freestanding 3D dendritic hierarchical porous Cu–Sn nanocomposites by chemically dealloying a designed $Cu_{35}Sn_{65}$ alloy with dendritic segregation. A 3D DHP Cu–Sn with electrodeposited polyaniline (PANI) further makes the nanocomposites with improved conductivity and structural stability, which are typical of bimodal pore size distribution composed of a dendritic micron-sized ligament-channel structure with interconnected nanoporous channel walls. When used as binder-free thick anodes for LIBs, the unique 3D DHP nanocomposites exhibit enhanced Li storage properties with ultrahigh first reversible capacity and initial CE, good cycling stability, and superior rate capability, which are mainly related to the unique 3D DHP structure, the moderate contact area between active materials and electrolytes, good buffer effect of inactive components,

and uniform coating of PANI nanolayers with good conductivity. Additionally, the Sn content and areal capacity of the 3D DHP electrode can be tuned by simply changing the dealloying time of the initial alloy, indicative of a promising 3D tin-based thick anode candidate with adjustable capacity toward high-performance LIBs.

2 | RESULTS AND DISCUSSION

2.1 | Microstructure and morphology characterization

Figure 1A shows the designed as-cast $Cu_{35}Sn_{65}$ alloy in the equilibrium phase diagram of the binary Cu–Sn system, which theoretically should be composed of Cu_6Sn_5 and Sn phases. As illustrated by XRD results in Figure 1B, the as-prepared $Cu_{35}Sn_{65}$ alloy mainly consists of two phases: Cu_6Sn_5 and Sn, and the amount of Cu_6Sn_5 is comparable to that of Sn in the Cu–Sn alloy. Note that a few Cu_3Sn phases can also be detected in the XRD results primarily because of the incomplete peritectic reaction occurring in the rapid cooling process. EDX results (Figure 1C,D) exhibit that the atomic percentage of Cu and Sn in the alloy was quite close to the designed composition, indicating that the Cu–Sn alloy can be used further in the following study. The element mapping displays the dendritic-like alternating distribution features of Cu and Sn elements, implying the occurrence of dendritic segregation in the as-cast alloy (Figure 1E,F). This is in good line with the metallographic and SEM observations in Figure 1G,H. Additionally, the line scan and selected-area EDX results in Figure 1I,J further confirm a few Cu_3Sn phases intermittently distributing in the center of the Cu_6Sn_5 phase, just corresponding to the dark gray areas in the backscattered electron SEM image, well demonstrating the typical incomplete peritectic transformation.

Figure 2A schematically shows the preparation processes of 3D DHP Cu–Sn and Cu–Sn/PANI nanocomposites. Briefly, the 3D DHP Cu–Sn nanocomposites can be obtained facilely by one-step chemical dealloying of the designed as-cast $Cu_{35}Sn_{65}$ alloy with dendritic segregation in a specific corrosive solution. Note that this is the first time to report on 3D tin-based nanocomposites by one-step chemical dealloying of the binary Cu–Sn system with a markedly small standard reversible potential difference (<500 mV) between Sn and Cu [−0.136 V (vs. SHE) for Sn/Sn^{2+} and 0.342 V (vs. SHE) for Cu/Cu^{2+}] to the best of our knowledge, in which the key is to screen the proper corrosive system matching well with the alloy system. Herein, we found that the specific mixture composed of 5 wt.% HF and 1 wt.% HNO_3 can be effective for the dealloying of the binary Cu–Sn system. Moreover, to stabilize the 3D nanostructure and improve the conductivity, PANI nanolayers were electrodeposited on the 3D DHP Cu−Sn nanocomposites by CV to create the 3D DHP Cu–Sn/PANI nanocomposites. Figure 2B,C illustrates the plane and sectional SEM images of 3D DHP Cu–Sn nanocomposites by dealloying for 12 h. It is obvious that the dendritic porous microstructure with aligned ligaments/channels in the microscale (ca. 20 μm) and ca. 200 μm in thickness can be observed in the as-dealloyed products. The high-magnification SEM images (insets of Figure 2B,C) further exhibit that the aligned micron-sized ligaments are composed of (rather than coated by) plenty of stacked NPs with adequate nanovoids around them. The specific surface area was evaluated based on N_2 adsorption/desorption experiments, as shown in Supporting Information: Figure S1A. The Brunauer–Emmett–Teller (BET) surface area of the 3D DHP nanocomposites can be determined to be $1.32 \pm 0.1\ m^2\ g^{-1}$. Note that this value is just between those of uniform microporous and nanoporous architectures reported in the literature,[43] which can be expected to not only provide enough electrochemical reaction active sites but effectively avoid the formation of overmuch SEI films and the occurrence of abundant side reactions on electrode surfaces by means of decreasing the contact area between the electrode and electrolyte when used as LIB anodes.[18] The pore size distribution curve ranging from 10 nm to 10 μm (Supporting Information: Figure S1B) by the mercury intrusion method displays one sharp peak centered at 893.24 nm, corresponding to the feature sizes of nanovoids in nanoporous channel walls. As a result, the 3D DHP Cu–Sn nanocomposites have typical bimodal pore size distribution comprising a dendritic micron-sized ligament-channel structure with interconnected nanoporous channel walls formed by plenty of NPs. EDX results (inset of Figure 2B) show a relatively high Sn content of 10.26 at.% in the as-dealloyed products, implying its promising high areal capacity in LIBs. Figure 2D,E further displays the 3D DHP Cu–Sn/PANI nanocomposites reserving similar structural features with the previous 3D DHP Cu–Sn counterpart after PANI electrodeposition, indicative of its good structure heredity and integrity during the electrodeposition. TEM observations (Figure 2F,G) illustrate that these NPs making up micron-sized channel walls possess feature sizes of ca. 500 nm and each NP was wrapped evenly by a conformal PANI layer with ca. 20 nm in thickness. XRD analysis (Figure 2H) further verifies that the as-dealloyed specimens are mainly composed of Cu, Cu_6Sn_5, and Cu_3Sn phases, in which Cu and Cu_6Sn_5 phases are highly predominant. Compared to the 3D DHP Cu–Sn

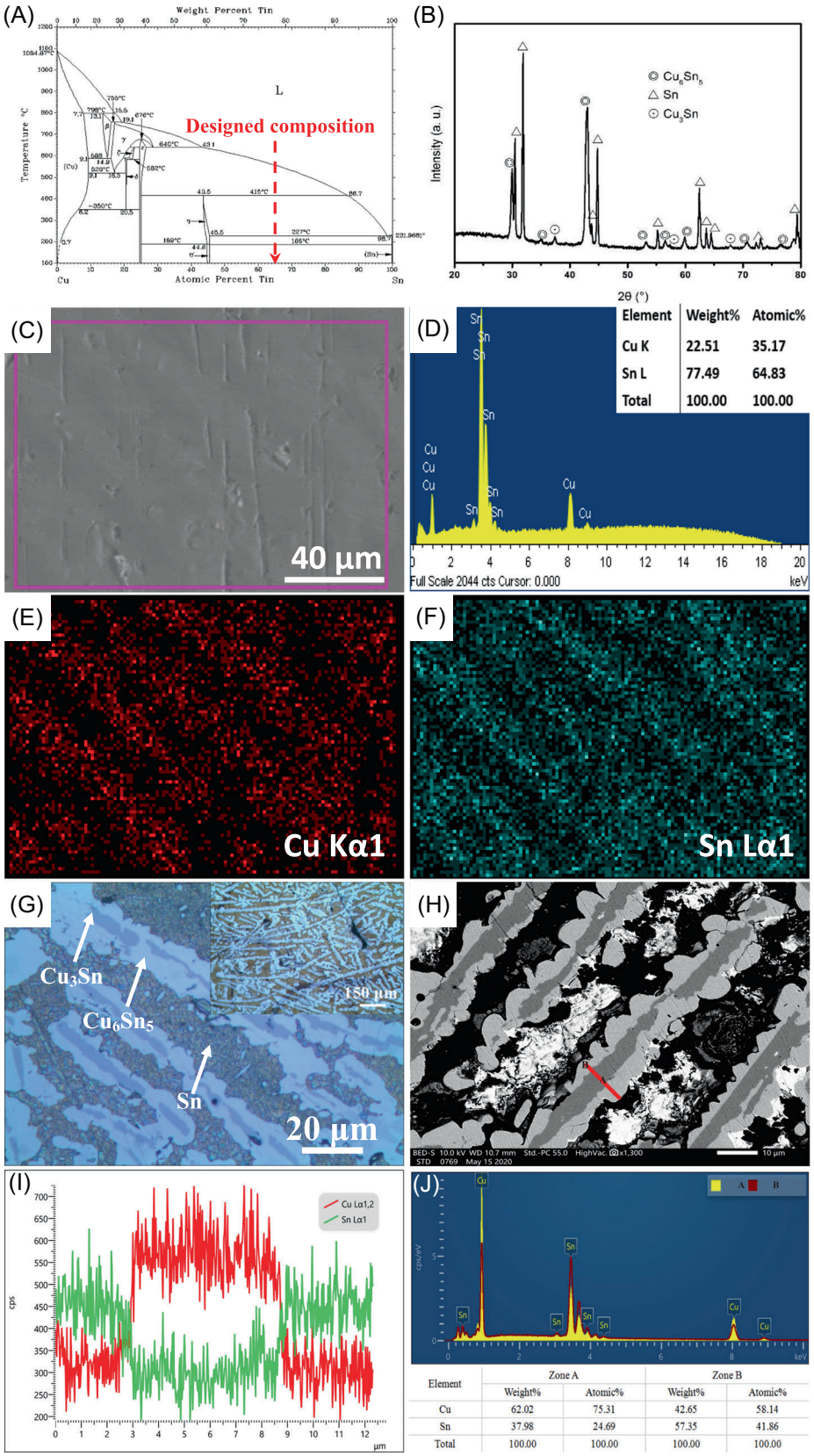

FIGURE 1 (A) Equilibrium phase diagram of the binary Cu–Sn system, in which the red dotted arrow shows the designed chemical composition of the Cu–Sn alloy in this study. (B) XRD pattern, (C) SEM image, (D) EDX results, and (E, F) element mapping of the designed as-cast $Cu_{35}Sn_{65}$ alloy. (G) Metallograph, (H) backscattered electron SEM image, (I) line scan, and (J) selected-area EDX results of the designed as-cast $Cu_{35}Sn_{65}$ alloy, in which the inset in part G is the corresponding low-magnification image.

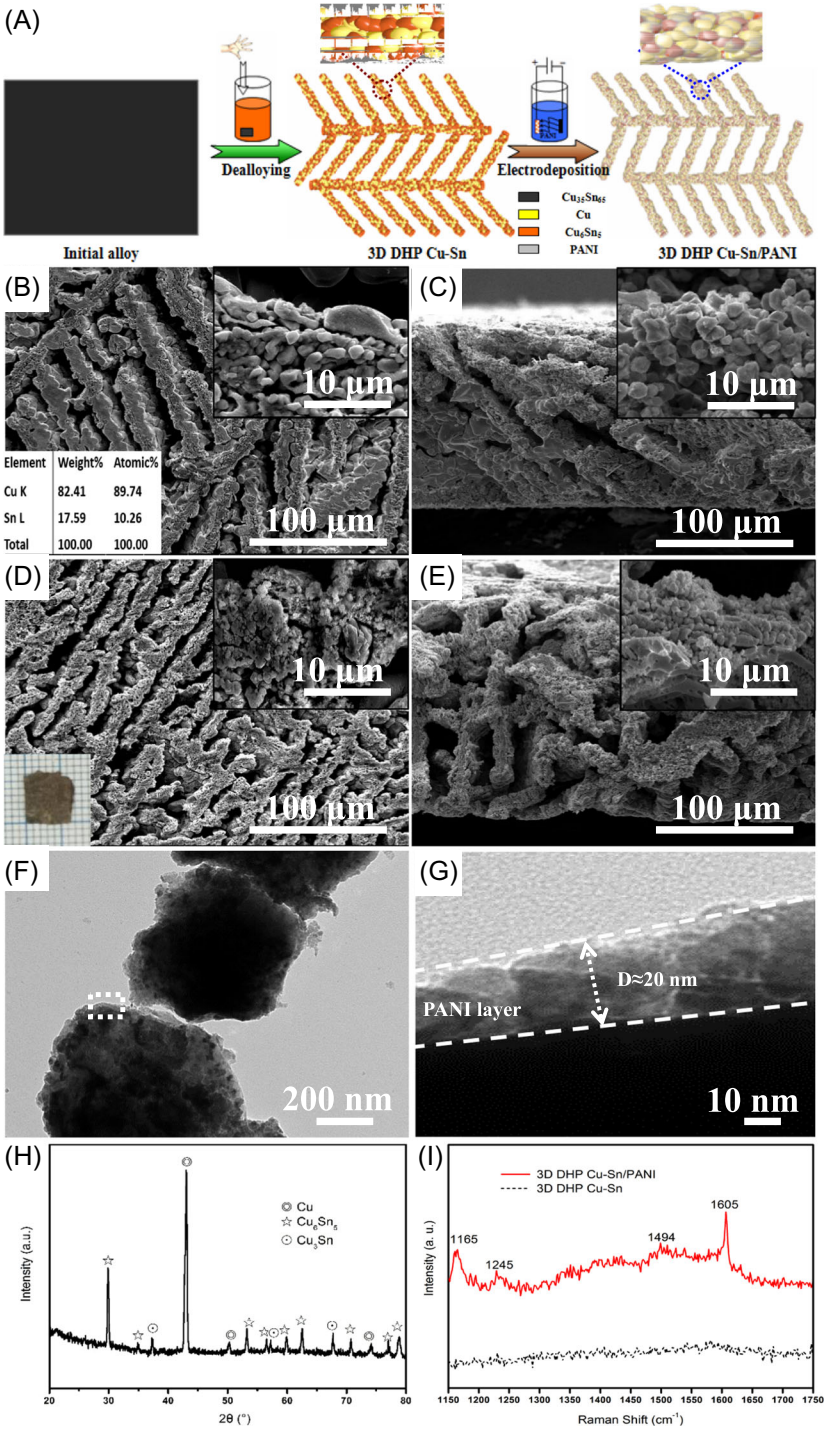

FIGURE 2 (A) Schematic of preparation processes of 3D DHP Cu–Sn and Cu–Sn/polyaniline (PANI) nanocomposites. (B, C) Plane and sectional SEM images of as-prepared 3D DHP Cu–Sn nanocomposites by chemical dealloying of the as-cast $Cu_{35}Sn_{65}$ alloy for 12 h. The inset at the left corner of part B is the corresponding chemical composition. (D, E) Plane and sectional SEM images of as-prepared 3D DHP Cu–Sn/PANI nanocomposites by PANI electrodeposition after dealloying for 12 h. The inset at the bottom-left corner of part D is a typical digital picture of synthetic products. The insets at the top-right corners of parts B–E are their local high-magnification images of micron-sized channel walls. (F) Typical TEM image of NPs making up the micron-sized channel walls in the 3D DHP Cu–Sn/PANI nanocomposites. (G) High-magnification TEM image of PANI nanolayers in the single NP surface, as marked by the white dotted rectangle in part F. (H) XRD pattern of the 12 h-dealloyed 3D DHP Cu–Sn nanocomposites. (I) Raman spectra of the 12 h-dealloyed 3D DHP Cu–Sn and Cu–Sn/PANI nanocomposites.

counterpart, Raman spectra of 3D DHP Cu–Sn/PANI nanocomposites have four characteristic peaks located at 1165, 1245, 1494, and 1605 cm^{-1}, designated to the typical C–H bending mode of the quinoid/benzenoid ring, weak C–H and C=N stretching modes of the quinoid ring, and the C–C stretching mode of the benzenoid ring in PANI, respectively.[44,45] In addition, element mapping results show the coexistence of C, N, Cu, and Sn elements in the 3D DHP Cu–Sn/PANI products as well as the uniform distribution of C and N on the micron-sized ligaments, further demonstrating the successful deposition of PANI (Supporting Information: Figure S2). Therefore, we can conclude that the 3D DHP Cu–Sn/PANI nanocomposites also possess bimodal pore size distribution composed of a dendritic micron-sized ligament-channel structure with interconnected nanoporous channel walls formed by plenty of PANI-modified Cu–Sn alloy NPs.

To further reveal the formation mechanism of 3D DHP Cu–Sn nanocomposites, the dealloying behavior of the as-cast $Cu_{35}Sn_{65}$ alloy with dendritic segregation from 4 to 24 h was investigated systematically, as illustrated in Figure 3. Expressly, when the dealloying time is just 4 h, the as-dealloyed specimens are composed of Cu, Cu_6Sn_5, and Cu_3Sn triphases. Combined with the SEM and XRD results of the as-cast Cu–Sn alloy, it is easy to understand that in this dealloying stage, the dendritic-like Sn phase in the as-cast alloy can be entirely dissolved to form the aligned micron-sized channels, while the main Cu_6Sn_5 and a few Cu_3Sn phases just may be selectively corroded to some extent due to the limited dealloying time, resulting in the formation of partial nanoporous copper in the micron-sized channel walls. Note that the Cu_6Sn_5 phase can be etched quicker than the Cu_3Sn due to its relatively high Sn content, and thus, the resultant dendritic nanoporous channel walls comprise Cu, Cu_6Sn_5, and Cu_3Sn triphases after dealloying for 4 h. With the increase of dealloying times, phase constitution of the as-dealloyed specimens varies gradually from Cu, Cu_6Sn_5, and Cu_3Sn triphases to Cu and Cu_6Sn_5 biphases, in which the amounts of Cu_6Sn_5 and Cu_3Sn phases decrease continually but the counterpart of Cu increases in proportion. Due to the amount of Cu_3Sn being far less than the Cu_6Sn_5 phase, just Cu and Cu_6Sn_5 biphases can be obtained finally in the 24 h-dealloyed specimens. It is interesting that no obvious morphology and microstructure changes can occur in these 3D DHP products that were subjected to different dealloying times except for the slight discrepancy in feature sizes and uniformity of NPs making up micron-sized channel walls. Typically, the ideal 3D DHP structure can be achieved as the dealloying time reaches 12 h or more. This is why the 12 h-dealloyed 3D DHP Cu–Sn/PANI nanocomposites can be selected preferentially as the research object. Figure 3I further shows the composition evolution of the as-cast $Cu_{35}Sn_{65}$ alloy with dealloying times as tested by EDX. Obviously, three composition regions, denoted by I, II, and III, can be distinguished. In region I, the atomic percentages of Cu and Sn alter dramatically, while those counterparts in region II spanning dealloying time from 4 to 12 h only change mildly; thereafter, a slighter composition variation can be found in region III. Note that as the dealloying time rises to 36 h, Sn atoms can be removed totally from the as-cast alloy, and the remaining Cu can be oxidized partially by the active oxygen radical (O·) in the solution, leading to the formation of 3D DHP Cu–Cu_2O nanocomposites with similar microstructure features as 3D DHP Cu–Sn counterparts (Supporting Information: Figure S3). Thus, it can be reasonable to conclude that the content of Sn in the 3D DHP Cu–Sn and Cu–Sn/PANI nanocomposites can be modulated easily in a broad composition range (0–25 at.% or 0–38.4 wt.%, where the 25 at.%/38.4 wt.% Sn corresponds to the dealloying for 4 h) through simply changing the dealloying time of the initial alloy.

2.2 | Electrochemical properties

To evaluate their merits in Li storage properties, the 12 h-dealloyed 3D DHP Cu–Sn and Cu–Sn/PANI nanocomposites with ca. 200 μm in thickness were preferentially served as LIB anodes to assemble directly into half-cells using metal Li foils as counter and reference electrodes without any binders and conductive agents. For comparison, the 2D copper foil-supported hierarchical porous Cu–Sn (2D HP Cu–Sn) electrode also composed of Cu and Cu_6Sn_5 biphases was introduced in some electrochemical tests, which can be obtained typically by electroless deposition of Sn on the 2D copper foil substrate in a Sn^{2+}-containing acidic plating solution at 45°C (see the supplementary information for the detailed experimental method, XRD, SEM, and EDX results, Supporting Information: Figure S4). Figure 4A shows the 1st-cycle CVs of the 12 h-dealloyed 3D DHP Cu–Sn/PANI electrode between 0.01 and 1.2 V (vs. Li/Li^+) at a scan rate of 0.1 mV s^{-1}, in which the open circuit voltage (OCV) is ca. 2.43 V (vs. Li/Li^+) and the inset is the local enlargement of the discharge process at the potential range of 0.3–1.2 V (vs. Li/Li^+). Obviously, in the 1st discharge process, three cathodic peaks at 1.26, 0.48, and below 0.3 V (vs. Li/Li^+) can be observed clearly, orderly corresponding to the formation of SEI films, as well as two-step phase conversions of Cu_6Sn_5 to Li_2CuSn and to Li_xSn, respectively.[23] It should be noted that the intensity of

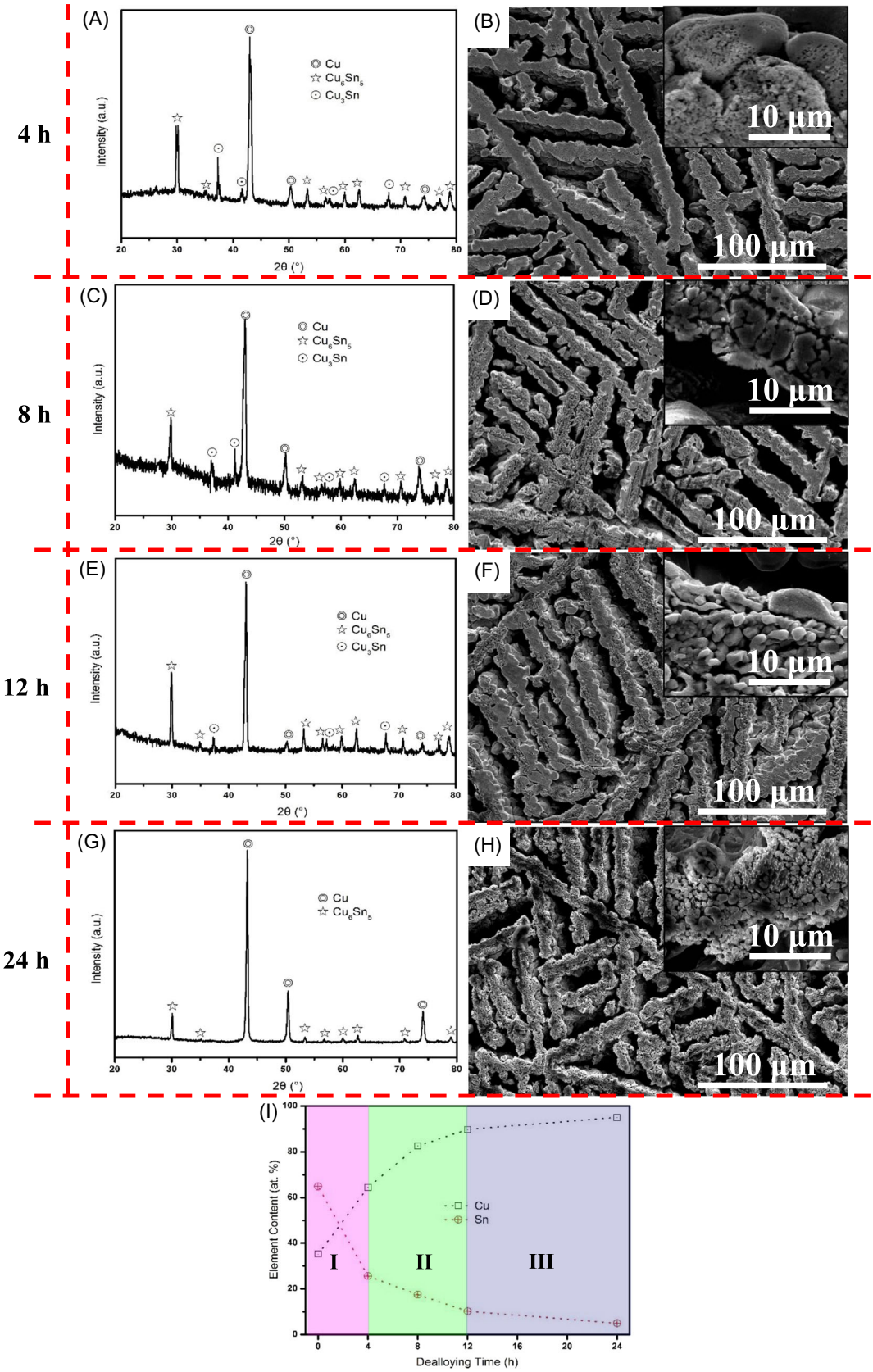

FIGURE 3 (A–H) XRD patterns and plane SEM images of 3D DHP Cu–Sn nanocomposites by chemical dealloying of the as-cast $Cu_{35}Sn_{65}$ alloy for 4, 8, 12, and 24 h. The insets at the top-right corners of parts B, D, F, and H are their local high-magnification images of micron-sized channel walls. (I) Chemical composition variation of the as-cast $Cu_{35}Sn_{65}$ alloy by dealloying for different times.

the cathodic peak at 1.26 V (vs. Li/Li$^+$) assigned to the SEI formation is quite weak, implying its high initial CE due to extremely limited Li$^+$ loss during the 1st discharge process. In fact, the designed 3D DHP structure with large-sized micropores and the limited contact area between the electrode and electrolyte can effectively avoid the formation of overmuch SEI films from the decomposition of the organic electrolyte and the occurrence of abundant side reactions on electrode surfaces compared to those uniform nanostructured electrodes with remarkably larger specific surface areas.[18,43] In addition, the as-prepared 3D DHP electrode without any binders and conductive agents also can reduce the occurrence of side reactions effectively on electrode surfaces, further improving the initial CE. In contrast, during the 1st charge process, there exist two anodic peaks located at 0.68 and

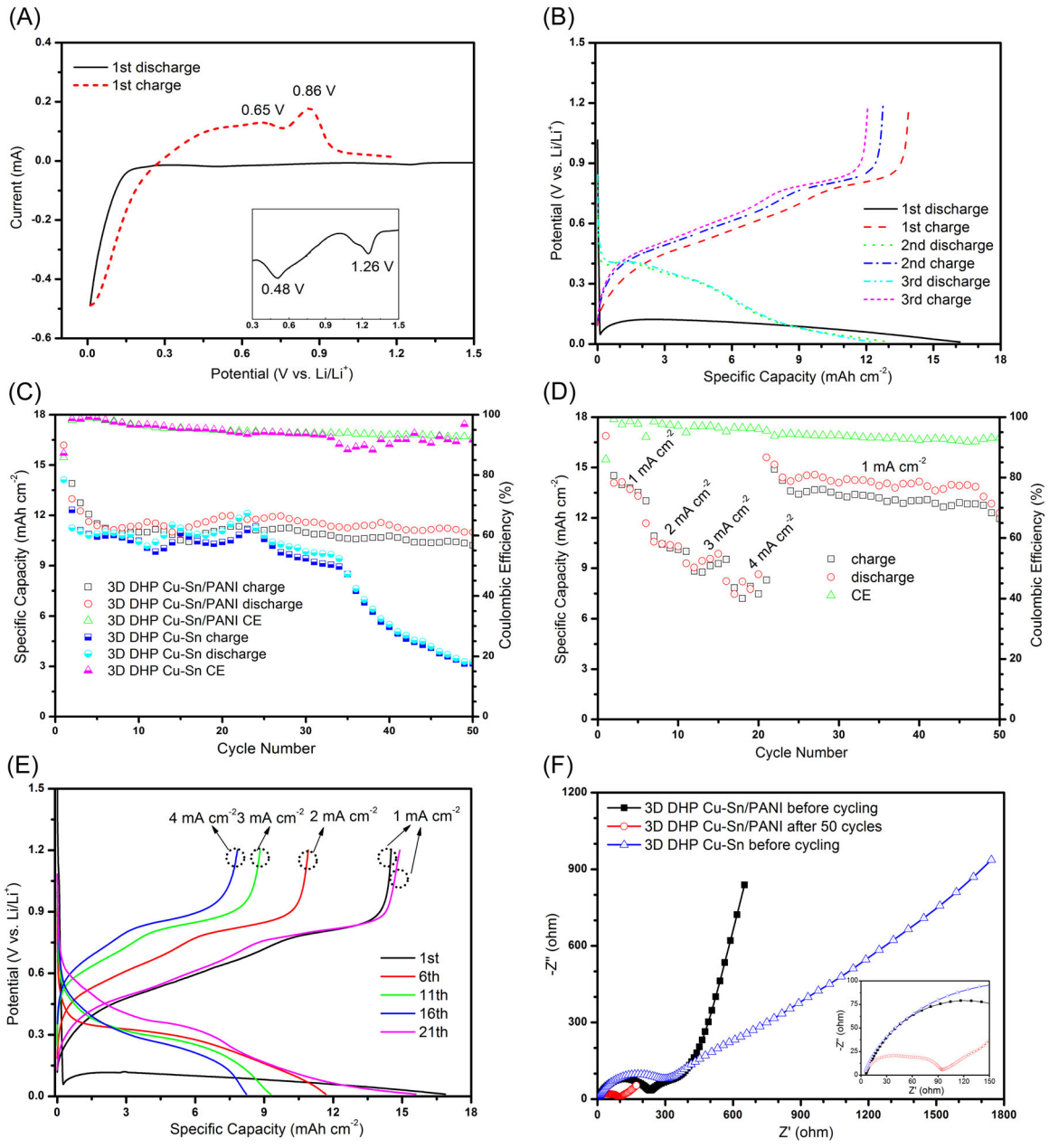

FIGURE 4 (A) CVs of the 12 h-dealloyed 3D DHP Cu–Sn/polyaniline (PANI) electrode ranging from 0.01 to 1.2 V (vs. Li/Li$^+$) at a scan rate of 0.1 mV s^{-1}. (B) Galvanostatic charge–discharge profiles of the 12 h-dealloyed 3D DHP Cu–Sn/PANI electrode at a current density of 1 mA cm^{-2}. (C) Cycle performance of the 12 h-dealloyed 3D DHP Cu–Sn and Cu–Sn/PANI electrodes at a current density of 1 mA cm^{-2}. (D) Rate capability of the 12 h-dealloyed 3D DHP Cu–Sn/PANI electrode at current densities of 1, 2, 3, and 4 mA cm^{-2}. (E) Potential versus capacity profiles of the 12 h-dealloyed 3D DHP Cu–Sn/PANI electrode under different current densities. (F) Nyquist plots of the 12 h-dealloyed 3D DHP Cu–Sn and Cu–Sn/PANI electrodes at different cycling states, in which the inset shows the local enlargement of the compressed semicircle at a high–medium frequency range.

0.90 V (vs. Li/Li^+), well corresponding to electrochemical delithiation reactions step by step from Li_xSn to Sn phase.[23] As we know, the subsequent charge and discharge cycles are typical electrochemical alloying and dealloying processes of Sn reacting with Li^+. The plenty of inactive component Cu produced in the 1st discharge process can serve as minicushions around Sn evenly to effectively relieve its volume expansion and particle aggregation during subsequent cycling, giving rise to the further improvement of the electrochemical performance of Sn. This is why the Cu_6Sn_5 alloy can be considered to be a more promising anode candidate compared to conventional Cu-supported/-doped Sn or other forms of Cu–Sn hybrids. The total electrochemical lithiation–delithiation reactions can be expressed in detail as follows[46,47]:

$$Cu_6Sn_5 + 10Li^+ + 10e^- \rightarrow 5Li_2CuSn + Cu \quad \text{(1st discharge)}, \tag{1}$$

$$Li_2CuSn + xLi^+ + xe^- \rightarrow Li_{2+x}Cu_{1-y}Sn + yCu \quad (0 < x < 2.4, 0 < y < 1, \text{1st discharge}), \tag{2}$$

$$Li_xSn \rightarrow Sn + xLi^+ + xe^- \quad (0 < x < 4.4, \text{1st and subsequent charge}), \tag{3}$$

$$Sn + xLi^+ + xe^- \rightarrow Li_xSn \quad (0 < x < 4.4, \text{discharge after 1st cycle}). \tag{4}$$

Figure 4B exhibits the galvanostatic charge–discharge profiles of the 12 h-dealloyed 3D DHP Cu–Sn/PANI electrode at a current density of 1 mA cm^{-2}. It is clear that the 1st discharge and charge processes deliver significantly large areal capacities of 16.18 and 13.89 mAh cm^{-2}, respectively, with initial CE as high as 85.8%, implying the markedly less irreversible Li^+ consumption during the 1st cycle, which is, to the best of our knowledge, rarely seen in common Sn-based electrodes.[28,36,38,48-54] Moreover, two obvious discharge and charge plateaus at ca. 0.1 and 0.7 V (vs. Li/Li^+) can be observed after the 1st cycle, assigning to the reversible electrochemical alloying and dealloying processes of Sn reacting with Li^+, as depicted by Equations (3) and (4). Note that the galvanostatic charge–discharge curves of the 12 h-dealloyed 3D DHP Cu–Sn electrode (Supporting Information: Figure S5) also possess a highly similar variation tendency (including a large discharge capacity of 14.12 mAh cm^{-2}, high initial CE of 87.2%, and comparable charge–discharge potential plateaus) with the 3D DHP Cu–Sn/PANI counterpart, demonstrating their same electrochemical reaction mechanisms during lithiation–delithiation processes and no additional impacts from PANI coating except for notably improved cycling stability.

Figure 4C shows the cycle performance of the 12 h-dealloyed 3D DHP Cu–Sn and Cu–Sn/PANI electrodes at a current density of 1 mA cm^{-2}. Evidently, both the 3D DHP electrodes with ultrahigh 1st reversible capacities display an initial capacity decline in the first several cycles, which is closely associated with the formation of SEI films, irreversible conversion of Cu_6Sn_5 to Li_xSn, and partial reversibility of Sn reacting with Li^+.[35] Except for the first several cycles, the 3D DHP Cu–Sn/PANI electrode still possesses a ultrahigh reversible capacity of 10.2 mAh cm^{-2} and a good cycling stability with 73.5% capacity retention after 50 cycles, indicating its excellent electrochemical reversibility. The SEM images and EDX results of the 3D DHP Cu–Sn/PANI electrode after cycling are further exhibited in Supporting Information: Figure S6. It is clear that there is no obvious difference in the microstructure and chemical composition between before and after cycling, demonstrating its good mechanical integrity and structural stability. This can be mainly attributed to the unique 3D DHP structure, good buffer effect of the inactive component, and uniform coating of the PANI nanolayer, which is conducive to alleviating the huge volume variation, enhancing the stability of SEI films, and improving the electron conductivity, thus enabling boosted Li storage performance. In contrast, the 3D DHP Cu–Sn electrode delivers the reversible capacities of 9.8 and 3.1 mAh cm^{-2} after 30 and 50 cycles, corresponding to only 69.4% and 25.7% capacity retention, respectively. Note that the reversible capacity of the 3D DHP Cu–Sn electrode drastically drops after 30 cycles, implying its relatively inferior structural stability under such an ultrahigh-capacity condition (high Sn content in essence). Even so, the Li storage properties (areal capacity, initial CE, and capacity retention) of the 3D DHP Cu–Sn electrode still are much better than those (1st reversible capacity of 0.44 mAh cm^{-2} with 71.5% CE and 21.8% capacity retention after 50 cycles) of the 2D HP Cu–Sn electrode with similar Sn content (9.75 at.% Sn), as presented in Supporting Information: Figure S7. The quite low areal capacity of the 2D HP electrode might be primarily attributed to the poor availability of Sn inside the electrode caused by unevenly hierarchical pore structure and ultrafine small-sized pores (<10 nm) severely preventing the organic electrolyte from permeation. Therefore, it can be concluded that the unique 3D DHP Cu–Sn/PANI electrode with high Sn content can act as a 3D thick anode toward high-performance LIBs, in which PANI coating effectively improves its structural stability and electrochemical reversibility.

Rate performance is another key assessment for the Li storage properties of LIBs. Figure 4D exhibits the rate capability of the 12 h-dealloyed 3D DHP Cu–Sn/PANI electrode under different current densities. Clearly, the pronounced large reversible capacities of 14.5, 10.9, 8.8, and 7.8 mAh cm^{-2} can be obtained at the current densities of 1, 2, 3, and 4 mA cm^{-2}, respectively. Impressively, when the current density returns to 1 mA cm^{-2} again at the 21st cycle, the reversible capacity promptly increases to 14.89 mAh cm^{-2}, retaining ca. 100% capacity retention compared to the 1st cycle at the same current density. Besides, after experiencing a succession of high-rate charge–discharge cycles, the ultrahigh reversible capacity of 11.95 mAh cm^{-2} still can be attained at the 50th cycle, indicating the excellent rate capability of the 3D DHP Cu–Sn/PANI electrode as a thick anode with high Sn content. Figure 4E further illustrates the potential versus capacity profiles of the 12 h-dealloyed 3D DHP Cu–Sn/PANI electrode under different current densities. Obviously, the curve variation tendency and lithiation–delithiation potential plateaus maintain well even though at higher current densities than the initial value; as the current density reverts to 1 mA cm^{-2} again, the charge capacity profile overlaps well with the 1st counterpart (including variation tendency, specific capacity, and potential plateau), implying its outstanding structural stability and electrochemical reversibility at higher rates. This is closely related to the unique 3D DHP structure with interconnected nanoporous channel walls formed by PANI-modified Cu–Sn alloy NPs, which provides the inherent benefits toward fast Li^+ and electron transports at electrode/electrolyte and current collector/active material interfaces in LIBs. This will be discussed further on a basis of the EIS results in the following part.

To clarify the Li^+ and electron-transport mechanism in the electrode, Nyquist plots of the 12 h-dealloyed 3D DHP Cu–Sn and Cu–Sn/PANI electrodes at different cycling states were further tested, as presented in Figure 4F. It is evident that all Nyquist plots consist of a compressed semicircle at a high–medium frequency range and an inclined line in the low-frequency range.[55,56] It has been well-recognized that the diameter of the compressed semicircle represents the charge transfer resistance (R_{ct}) depending on electrochemical reactions happening at electrode/electrolyte interfaces, and the slope of the inclined line is closely associated with the Li^+ diffusion rate inside electrode materials.[18,21,57] Clearly, the R_{ct} value of the 3D DHP Cu–Sn/PANI electrode before cycling is ca. 250 Ω, slightly lower than that (ca. 350 Ω) of the 3D DHP Cu–Sn electrode but much lower than that (ca. 600 Ω, Supporting Information: Figure S8) of the 2D HP Cu–Sn electrode, indicating its better electron conductivity by the uniform coating of the PANI nanolayer. Note that the R_{ct} of the 3D DHP Cu–Sn/PANI electrode after 50 cycles reduces prominently and can be identified to be just 93.5 Ω by equivalent circuit fitting of EIS (Supporting Information: Figure S9 and Note 1), fully demonstrating the excellent Li^+/electron transport ability and good electrode/electrolyte wettability in the 3D DHP Cu–Sn/PANI electrode.

To further verify its adjustable capacity feature by simply changing the dealloying time of the initial alloy, the 24 h-dealloyed 3D DHP Cu–Sn nanocomposites (Figure 3H) were served as a typical model to carry out the PANI electrodeposition under the same condition, resulting in the formation of 3D DHP Cu–Sn/PANI nanocomposites with 5 at.% Sn, as displayed in Figure 5A–D. Clearly, the plane and sectional microstructures of the 3D DHP nanocomposites after the electrodeposition (Figure 5C,D) have quite similar configurations with the 24 h-dealloyed 3D DHP Cu–Sn counterpart (Figure 5A,B) except for a slight reduction in the feature sizes of micron-sized channel walls, indicating the good microstructure inheritance after electrodeposition. Moreover, the resistivity of the 24 h-dealloyed 3D DHP Cu–Sn and Cu–Sn/PANI nanocomposites was further tested using a four-point probe method (see Note 2 in the Supplementary Material for measurement details). Obviously, the 3D DHP Cu–Sn/PANI nanocomposite (just 2.71×10^{-7} Ω·m) has markedly lower resistivity than the 3D DHP Cu–Sn counterpart (5.08×10^{-6} Ω·m), confirming that PANI coatings effectively improve the electron conductivity of the 3D DHP Cu–Sn nanocomposites. Figure 5E displays the cycle performance of the 24 h-dealloyed 3D DHP Cu–Sn and Cu–Sn/PANI electrodes at 1 mA cm^{-2}. As can be seen clearly, the 1st reversible capacities of both the 3D DHP electrodes can be determined to be 2.78 and 3.11 mAh cm^{-2}, approximately one-fourth less than those counterparts by dealloying just for 12 h, manifesting the favorable achievement of capacity modulation in the 3D DHP electrodes by simply changing the dealloying time of the initial alloy. Moreover, the cycling stability of both the 3D DHP electrodes also can be improved largely relative to the just 12 h-dealloyed counterparts (Figure 4C). Typically, the 24 h-dealloyed 3D DHP Cu–Sn/PANI electrode delivers the reversible capacities of 2.45 and 1.98 mAh cm^{-2} after 50 and 100 cycles, maintaining the high capacity retention of 78.8% and 63.8%, respectively. The SEM images of the 24 h-dealloyed 3D DHP Cu–Sn/PANI electrode after 100 cycles are further shown in Supporting Information: Figure S10. Obviously, the intact dendritic hierarchical

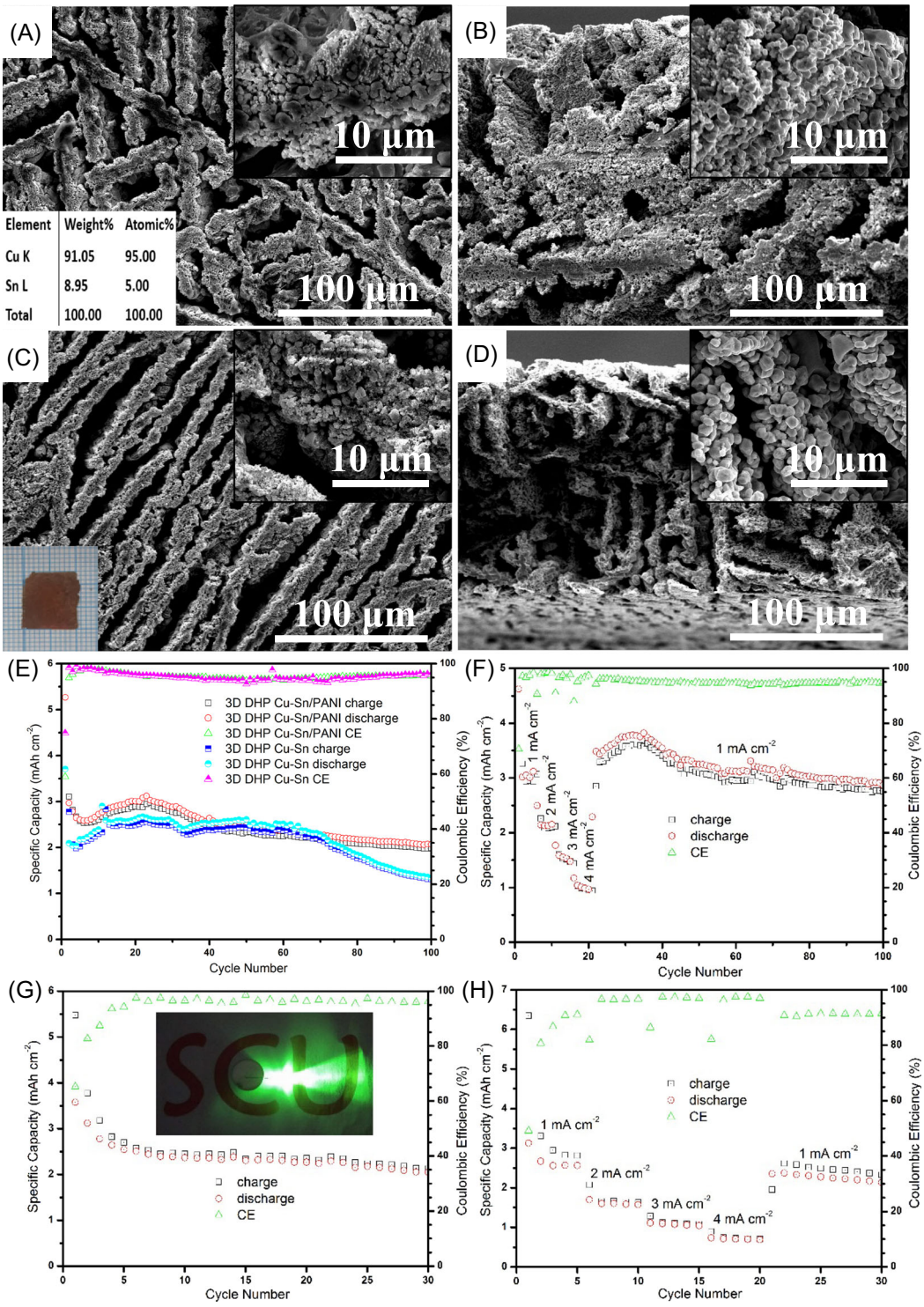

FIGURE 5 (A, B) Plane and sectional SEM images of as-prepared 3D DHP Cu–Sn nanocomposites by chemical dealloying of the as-cast $Cu_{35}Sn_{65}$ alloy for 24 h. The inset at the left corner of part a is the corresponding chemical composition. (C, D) Plane and sectional SEM images of as-prepared 3D DHP Cu–Sn/PANI nanocomposites by PANI electrodeposition after the dealloying for 24 h. The inset at the bottom-left corner of part C is a typical digital picture of synthetic products. The insets at the top-right corners of parts A–D are their local high-magnification images of micron-sized channel walls. (E) Cycle performance of the 24 h-dealloyed 3D DHP Cu–Sn and Cu–Sn/PANI electrodes at a current density of 1 mA cm^{-2}. (F) Rate capability of the 24 h-dealloyed 3D DHP Cu–Sn/PANI electrode at current densities of 1, 2, 3, and 4 mA cm^{-2}. (G) Cycle performance of the 3D DHP Cu–Sn/PANI//$LiCoO_2$ full cell at a current density of 1 mA cm^{-2}, in which the inset shows a digital image of LED powered by the assembled full cell with the full-charged state after 30 cycles. (H) Rate capability of the 3D DHP Cu–Sn/PANI//$LiCoO_2$ full cell at current densities of 1, 2, 3, and 4 mA cm^{-2}.

porous structure still can be observed clearly after cycling, which has little difference from the counterpart before cycling, fully demonstrating its good structural stability. Even if for the 24 h-dealloyed 3D DHP Cu–Sn electrode without PANI coatings, the reversible capacity of 1.3 mAh cm^{-2} still can be obtained after 100 cycles with ca. 46.9% capacity retention, better than the 12 h-dealloyed counterpart, implying the relatively poor cycling stability occurring in high-capacity 3D tin-based electrodes. This is mainly because the higher Sn loadings in 3D electrodes are prone to give rise to larger volume and structure changes as well as an insufficient cushion of mechanical strain in the unit area during repeated lithiation–delithiation processes, easily leading to serious cracking, pulverization, and detachment of active materials from electrode surfaces. A detailed comparison of Li storage properties of 3D DHP Cu–Sn/PANI electrodes prepared by dealloying for different times with other tin-based electrode materials reported in the recent literature has been performed, as listed in Supporting Information: Table S1. Evidently, the boosted areal capacity and prolonged cycle life can be achieved smoothly in the 3D DHP Cu–Sn/PANI electrode, especially at high current densities. Additionally, the 24 h-dealloyed 3D DHP Cu–Sn/PANI electrode displays superior rate capability, as shown in Figure 5F. The reversible capacities of 3.26, 2.26, 1.61, and 1.03 mAh cm^{-2} can be reached in turn at the current densities of 1, 2, 3, and 4 mA cm^{-2}, respectively. As the current density went back to 1 mA cm^{-2} again, a high reversible capacity of 2.75 mAh cm^{-2} still can be attained after 100 charge–discharge cycles, retaining as high as 84.3% capacity retention in comparison with the 1st cycle, demonstrating its outstanding rate performance. Note that a slight capacity increase can be observed from the 21st to 30th cycles, which is likely attributed to the more active material inside the electrode reacting with Li^+ sufficiently by the boosted reaction kinetics at the low current density.[58,59] These results further confirm that the capacity modulation of the as-prepared 3D DHP electrode can be achieved effectively in a broad capacity range by a rational dealloying strategy.

Besides, the 24 h-dealloyed 3D DHP Cu–Sn/PANI electrode as a binder-free thick anode was also assembled into Li-ion full cells using commercial $LiCoO_2$ as a cathode to further demonstrate its suitability toward practical applications of LIBs. Figure 5G,H shows the typical electrochemical properties of the 3D DHP Cu–Sn/PANI//$LiCoO_2$ full cells tested in a voltage range of 2.5–4.2 V. As indicated in Figure 5G, the cycle performance curve exhibits the large 1st reversible capacity of 3.57 mAh cm^{-2} with relatively high initial CE of 65.27% at a current density of 1 mA cm^{-2}; after 30 charge–discharge cycles, the reversible capacity of 2.12 mAh cm^{-2} still can be reached with 58% capacity retention, indicating its good cycling stability. A typical digital photograph of a light-emitting diode (LED) powered by the full cell with the full-charged state after 30 cycles is presented in the inset of Figure 5G, further verifying its promising applicability in microelectronic devices. Besides, the rate capability of the 3D DHP Cu–Sn/PANI//$LiCoO_2$ full cell was investigated in Figure 5H. Clearly, the relatively large reversible capacities of 2.56, 1.57, 1.04, and 0.68 mAh cm^{-2} can be obtained after every five cycles at the current densities of 1, 2, 3, and 4 mA cm^{-2}, respectively. When the current density gets back to 1 mA cm^{-2}, the reversible capacity increases to 2.35 mAh cm^{-2} quickly, maintaining as high as 91.8% capacity retention in comparison with that of the 5th cycle at the same current density. Note that after enduring a series of high-rate cycling, the assembled full cell still can deliver the reversible capacity of 2.13 mAh cm^{-2} after 30 charge–discharge cycles, certifying its good rate performance. Compared to other tin-based electrode materials with different structure designs in the literature, the enhanced Li storage performance of the as-prepared 3D DHP Cu–Sn/PANI thick anode with adjustable capacity can be mainly attributed to the following: (1) The designed 3D porous framework composed of (rather than coated by) Cu–Sn alloy NPs can remarkably enhance its specific capacity at unit area due to ultrahigh Sn content inside the electrode and meanwhile improve the chemical microenvironment between the current collector/active material interface by small-size and surface–interface synergistic effects. (2) The unique 3D DHP structure not only greatly facilitates the quick penetration of the organic electrolyte throughout the entire electrode but also can significantly reduce the diffusion distance of Li^+ between the electrode and electrolyte, resulting in the fast Li^+ transport ability. (3) Ample nanovoids among Cu–Sn alloy NPs and inert Cu as the cushion component can effectively accommodate huge volume and structure changes during repeated lithiation–delithiation processes, leading to good structural integrity. (4) The PANI nanolayer on Cu–Sn alloy NPs can form 3D nanosized conductive networks as high-efficient electron-transfer pathways inside electrode materials and meanwhile improve the structural stability of the electrode. (5) The addition of no binders and conductive agents is beneficial for the further enhancement of energy and power densities of full cells. Besides, the Sn content of the 3D DHP Cu–Sn/PANI electrode can be modulated easily in a wide composition range from several to tens of at.% and the corresponding areal capacity can be adjusted in a broad capacity region from several to a dozen of mAh cm^{-2} by simply changing the dealloying time of the initial alloy, which can be

anticipated to greatly expand their possibility and flexibility of application in an emerging industry. Therefore, we believe that the present work provides a new design concept for promising 3D metal-based thick anodes with high active material loadings and wide adjustable capacity ranges in next-generation LIBs.

3 | CONCLUSIONS

In summary, a facile and effective one-step strategy has been developed to fabricate freestanding 3D DHP Cu–Sn nanocomposites by chemically dealloying an as-cast $Cu_{35}Sn_{65}$ alloy with dendritic segregation. A 3D DHP Cu–Sn modified by PANI further makes the nanocomposites with improved conductivity and structural stability, which are typical of bimodal pore-size distribution composed of a dendritic micron-sized ligament-channel structure with interconnected nanoporous channel walls formed by plenty of PANI-modified Cu–Sn alloy NPs. When used as binder-free thick anodes for LIBs, the 12 h-dealloyed 3D DHP Cu–Sn/PANI nanocomposites exhibit enhanced Li storage performance with a first reversible capacity of 13.9 mAh cm^{-2}, initial CE of 85.8%, capacity retention of 73.5% after 50 cycles, and superior rate capability with a reversible capacity of 11.95 mAh cm^{-2} after a series of high-rate cycles. This can be largely ascribed to the unique 3D DHP structure, the moderate contact area between active materials and electrolytes, good buffer effect of inactive components, and uniform coating of PANI nanolayers with good conductivity, which facilitates alleviating the huge volume variation, enhancing the loading of active materials, strengthening the stability of SEI films, shortening the Li^+ diffusion length, and improving the electron conductivity. Besides, the Sn content in the 3D DHP electrode and its corresponding areal capacity can be tuned easily by simply changing the dealloying time of the initial alloy. We believe that this present work has an important implication for the design and fabrication of 3D metal-based thick electrodes with high active material loadings and wide adjustable capacity ranges toward practical applications of advanced electrochemical storage devices.

ACKNOWLEDGMENTS

This study was financially supported by the National Natural Science Foundation of China (52075351, 51604177), the National Key Research and Development Program of China (2019YFA0705701), the International S&T Innovation Cooperation Program of Sichuan Province (2020YFH0039), the Chengdu International S&T Cooperation Funded Project (2020-GH02-00006-HZ, 2022-GH02-00027-HZ), the "1000 Talents Plan" of Sichuan Province, the Experimental Technology Project of Sichuan University (SCU201078), and the Talent Introduction Program of Sichuan University (YJ201410).

CONFLICT OF INTEREST

The authors declare no conflict of interest.

DATA AVAILABILITY STATEMENT

The data that support the findings of this study are available from the corresponding author upon reasonable request.

ORCID

Wenbo Liu http://orcid.org/0000-0001-5636-5461

REFERENCES

1. Li CP, Xie XS, Liang SQ, Zhou J. Issues and future perspective on zinc metal anode for rechargeable aqueous zinc-ion batteries. *Energy Environ Mater*. 2020;3(2):146-159.
2. Yu F, Li SZ, Chen WR, Wu T, Peng C. Biomass-derived materials for electrochemical energy storage and conversion: overview and perspectives. *Energy Environ Mater*. 2019;2(1):55-67.
3. Nitta N, Wu FX, Lee JT, Yushin G. Li-ion battery materials: present and future. *Mater Today*. 2015;18(5):252-264.
4. Huang ZD, Zhang TT, Lu H, et al. Bimetal-organic-framework derived $CoTiO_3$ mesoporous micro-prisms anode for superior stable power sodium ion batteries. *Sci China Mater*. 2018;61(8):1057-1066.
5. Huang ZD, Yang MT, Qi JQ, et al. Mitigating the polysulfides "shuttling" with TiO_2 nanowires/nanosheets hybrid modified separators for robust lithium-sulfur batteries. *Chem Eng J*. 2020;387:124080.
6. Grey CP, Tarascon JM. Sustainability and in situ monitoring in battery development. *Nat Mater*. 2017;16(1):45-56.
7. Cao YQ, Meng XB, Li AD. Atomic layer deposition of high-capacity anodes for next-generation lithium-ion batteries and beyond. *Energy Environ Mater*. 2021;4(3):363-391.
8. Fang ZH, Wang J, Wu HC, Li QQ, Fan SS, Wang JP. Progress and challenges of flexible lithium ion batteries. *J Power Sources*. 2020;454:227932.
9. Armand M, Tarascon JM. Building better batteries. *Nature*. 2008;451:652-657.
10. Zhou L, Zhang K, Hu Z, et al. Recent developments on and prospects for electrode materials with hierarchical structures for lithium-ion batteries. *Adv Energy Mater*. 2018;8(6):1701415.
11. Zhou FC, Ouyang LZ, Liu JW, Yang XS, Zhu M. Chemical bonding black phosphorus with TiO_2 and carbon toward high-performance lithium storage. *J Power Sources*. 2020;449:227549.
12. Tarascon JM, Armand M. Issues and challenges facing rechargeable lithium batteries. *Nature*. 2001;414:359-367.
13. Palacín MR, Guibert AD. Why do batteries fail? *Science*. 2016;351:1253292.
14. Han Y, Huang GY, Xu SM. Structural reorganization-based nanomaterials as anodes for lithium-ion batteries: design, preparation, and performance. *Small*. 2019;16(15):1902841.
15. Zhang FC, Wang Y, Guo WB, Rao S, Mao PY. Synthesis of Sn-MnO@nitrogen-doped carbon yolk-shelled three-dimensional

interconnected networks as a high-performance anode material for lithium-ion batteries. *Chem Eng J*. 2019;360:1509-1516.
16. Kwon JY, Ryu JH, Jung YS, Oh SM. Thermo-electrochemical activation of Cu_3Sn negative electrode for lithium-ion batteries. *J Alloys Compd*. 2011;509(28):7595-7599.
17. Shi HX, Fang ZW, Zhang X, et al. Double-network nanostructured hydrogel-derived ultrafine Sn-Fe alloy in three-dimensional carbon framework for enhanced lithium storage. *Nano Lett*. 2018;18(5):3193-3198.
18. Luo Z, Xu JC, Yuan B, et al. 3D hierarchical porous Cu-based composite current collector with enhanced ligaments for notably improved cycle stability of Sn anode in Li-ion batteries. *ACS Appl Mater Interfaces*. 2018;10:22050-22058.
19. Bazin L, Mitra S, Taberna PL, et al. High rate capability pure Sn-based nano-architectured electrode assembly for rechargeable lithium batteries. *J Power Sources*. 2009;188(2):578-582.
20. Nithyadharseni P, Reddy MV, Nalini B, Kalpana M, Chowdari BVR. Sn-based intermetallic alloy anode materials for the application of lithium ion batteries. *Electrochim Acta*. 2015;161:261-268.
21. Uysal M, Cetinkaya T, Alp A, Akbulut H. Active and inactive buffering effect on the electrochemical behavior of Sn-Ni/MWCNT composite anodes prepared by pulse electrodeposition for lithium-ion batteries. *J Alloys Compd*. 2015;645:235-242.
22. Ebner M, Marone F, Stampanoni M, Wood V. Visualization and quantification of electrochemical and mechanical degradation in Li ion batteries. *Science*. 2013;342:716-720.
23. Han QG, Yi Z, Cheng Y, Wu YM, Wang LM. Simple preparation of Cu_6Sn_5/Sn composites as anode materials for lithium-ion batteries. *RSC Adv*. 2016;6:15379-15285.
24. Liu WB, Zhang SC, Li N, An SS, Zheng JW. Preparation and characterization of sandwich-typed three-dimensional nanoporous copper-supported tin thin-film anode for lithium ion battery. *Int J Electrochem Sci*. 2013;8:347-358.
25. Liu WB, Chen X, Zhang JZ, Zhang SC, Shi SQ. In-situ synthesis of freestanding porous SnO_x-decorated Ni_3Sn_2 composites with enhanced Li storage properties. *Chem Eng J*. 2021;412:128591.
26. Ren W, Kong DZ, Cheng CW. Three-dimensional tin nanoparticles embedded in carbon nanotubes on carbon cloth as a flexible anode for lithium-ion batteries. *ChemElectroChem*. 2014;1:2064-2069.
27. Wu XM, Zhang SC, Fang H, Du ZJ, Lin RX. Feasibility of utilizing three-dimensional nanoarchitecture to endow metal sulfides with superior Li^+ storage capability. *J Power Sources*. 2014;264:311-319.
28. Hassoun J, Panero S, Simon P, Taberna PL, Scrosati B. High-rate, long-life Ni-Sn nanostructured electrodes for lithium-ion batteries. *Adv Mater*. 2007;19(12):1632-1635.
29. Yu Y, Gu L, Lang XY, et al. Li storage in 3D nanoporous Au-supported nanocrystalline tin. *Adv Mater*. 2011;23(21):2443-2447.
30. Ye X, Lin Z, Liang S, et al. Upcycling of electroplating sludge into ultrafine Sn@C nanorods with highly stable lithium storage performance. *Nano Lett*. 2019;19:1860-1866.
31. Liu WB, Chen L, Cui L, Yan JZ, Zhang SC, Shi SQ. Freestanding 3D nanoporous Cu@1D Cu_2O nanowire heterostructure: from facile one-step protocol to robust application in Li storage. *J Mater Chem A*. 2019;7:15089-15100.
32. Liu WB, Zhang SC, Li N, Zheng JW, An SS, Li GX. Influence of dealloying solution on the microstructure of monolithic nanoporous copper through chemical dealloying of Al 30 at.% Cu alloy. *Int J Electrochem Sci*. 2012;7:7993-8006.
33. Liu WB, Zhang SC, Li N, Zheng JW, An SS, Xing YL. Monolithic nanoporous copper ribbons from Mg-Cu alloys with copper contents below 33 at.%: fabrication, structure evolution and coarsening behavior along the thickness direction. *Int J Electrochem Sci*. 2011;6:5445-5461.
34. Zhang SC, Xing YL, Tao J, et al. A three-dimensional tin-coated nanoporous copper for lithium-ion battery anodes. *J Power Sources*. 2011;196(16):6915-6919.
35. Liu WB, Chen X, Xiang P, et al. Chemically monodisperse tin nanoparticles on monolithic 3D nanoporous copper for lithium ion battery anodes with ultralong cycle life and stable lithium storage properties. *Nanoscale*. 2019;11:4885-4894.
36. Liang J, Lu Y, Liu Y, et al. Oxides overlayer confined Ni_3Sn_2 alloy enable enhanced lithium storage performance. *J Power Sources*. 2019;441:227185.
37. Tan XF, McDonald SD, Gu Q, Wang L, Matsumura S, Nogita K. The effects of Ni on inhibiting the separation of Cu during the lithiation of Cu_6Sn_5 lithium-ion battery anodes. *J Power Sources*. 2019;440:227085.
38. Wang S, Yi Z, Wang X, Sun Q, Cheng Y, Wang L. A rational design to buffer volume expansion of CoSn intermetallic in lithium and sodium storage: multicore-shell versus monocore-shell. *Energy Storage Mater*. 2019;23:629-635.
39. Liu RQ, Lia DY, Wang C, et al. Core-shell structured hollow SnO_2-polypyrrole nanocomposite anodes with enhanced cyclic performance for lithium-ion batteries. *Nano Energy*. 2014;6:73-81.
40. Xu WW, Zhao KN, Niu CJ, et al. Heterogeneous branched core-shell SnO_2-PANI nanorod arrays with mechanical integrity and three dimentional electron transport for lithium batteries. *Nano Energy*. 2014;8:196-204.
41. Ding HM, Jiang H, Zhu ZJ, Hu YJ, Gu F, Li CZ. Ternary SnO_2@PANI/rGO nanohybrids as excellent anode materials for lithium-ion batteries. *Electrochim Acta*. 2015;157:205-210.
42. Wu H, Yu GH, Pan LJ, et al. Stable Li-ion battery anodes by in-situ polymerization of conducting hydrogel to conformally coat silicon nanoparticles. *Nat Commun*. 2013;4:1943.
43. Liu WB, Zhang SC, Li N, Zheng JW, Xing YL. A facile one-pot route to fabricate nanoporous copper with controlled hierarchical pore size distributions through chemical dealloying of Al-Cu alloy in an alkaline solution. *Micropor Mesopor Mater*. 2011;138(1-3):1-7.
44. Jeong JM, Choi BG, Lee SC, et al. Hierarchical hollow spheres of Fe_2O_3@Polyaniline for lithium ion battery anodes. *Adv Mater*. 2013;25:6250-6255.
45. Drury A, Chaure S, Kroll M, Nicolosi V, Chaure N, Blau WJ. Fabrication and characterization of silver/polyaniline composite nanowires in porous anodic alumina. *Chem Mater*. 2007;19:4252-4258.
46. Luo Z, Xu JC, Yuan B, et al. A novel 3D bimodal porous current collector with large interconnected spherical channels for improved capacity and cycling stability of Sn anode in Li-ion batteries. *Mater Lett*. 2018;213:189-192.
47. Wu XM, Zhang SC, Qi T, Fang H, Liu GR, Xing YL. Novel insight toward engineering of arrayed Cu@Sn nanoelectrodes:

rational microstructure refinement and its remarkable "harvesting effect" on lithium storage capability. *J Power Sources*. 2016;307:753-761.

48. Kong XG, Zhang JR, Huang JF, et al. Microwave assisted hydrothermal synthesis of tin niobates nanosheets with high cycle stability as lithium-ion battery anodes. *Chin Chem Lett*. 2019;30:771-774.
49. Yang J, Zhang JM, Zhou XY, Ren RP, Jiang M, Tang JJ. Sn-Co nanoalloys encapsulated in N-doped carbon hollow cubes as a high-performance anode material for lithium-ion batteries. *ACS Appl Mater Interfaces*. 2018;10:35216-35223.
50. Pan QC, Wu YN, Zhong WT, et al. Carbon nanosheets encapsulated NiSb nanoparticles as advanced anode materials for lithium-ion batteries. *Energy Environ Mater*. 2020;3(2):186-191.
51. Hassoun J, Derrien G, Panero S, Scrosati B. A nano-structured Sn-C composite lithium battery electrode with unique stability and high electrochemical performance. *Adv Mater*. 2008;20(16):3169-3175.
52. Lin M, Cheng DL, Liu JW, et al. Dual-carbon-confined SnS nanostructure with high capacity and long cycle life for lithium-ion batteries. *Energy Environ Mater*. 2021;4(4):562-568.
53. Liu WB, Lu BB, Liu XJ, Gan Y, Zhang SC, Shi SQ. In-situ synthesis of the peapod-like Cu-SnO_2@copper foam as anode with excellent cycle stability and high area specific capacity. *Adv Funct Mater*. 2021;31(33):2101999.
54. Yang SL, Zhou BH, Lei M, et al. Sub-100 nm hollow SnO_2@C nanoparticles as anode material for lithium ion batteries and significantly enhanced cycle performances. *Chin Chem Lett*. 2015;26:1293-1297.
55. Huang ZD, Zhang K, Zhang TT, et al. Hierarchical dispersed multi-phase nickel cobalt oxide mesoporous thorn microspheres as superior rate anode materials for lithium ion batteries. *J Mater Chem A*. 2015;3(42):20886-20891.
56. Xu QT, Xue HG, Guo SP. FeS_2 walnut-like microspheres wrapped with rGO as anode material for high-capacity and long-cycle lithium-ion batteries. *Electrochim Acta*. 2018;292:1-9.
57. Guo SP, Li JC, Xiao JR, Xue HG. Fe_3S_4 nanoparticles wrapped in an rGO matrix for promising energy storage: outstanding cyclic and rate performance. *ACS Appl Mater Interfaces*. 2017;9(43):37694-37701.
58. Xu QT, Xue HG, Guo SP. Facile preparation of FeS@GO and its outstanding electrochemical performances for lithium storage. *Inorg Chem Front*. 2018;5(10):2540-2545.
59. Xu QT, Li JC, Xue HG, Guo SP. Effective combination of FeS_2 microspheres and Fe_3S_4 microcubes with rGO as anode material for high-capacity and long-cycle lithium-ion batteries. *J Power Sources*. 2018;396:675-682.

SUPPORTING INFORMATION

Additional supporting information can be found online in the Supporting Information section at the end of this article.

How to cite this article: Liu W, Gou H, Dong X, Zhang S, Shi S. Rational design of PANI-modified three-dimensional dendritic hierarchical porous Cu–Sn nanocomposites as thick anodes with ultrahigh areal capacity and good cycling stability. *Battery Energy*. 2023;2:20220032. doi:10.1002/bte2.20220032